Repositorio Institucional de la Universidad Autónoma de Madrid

https://repositorio.uam.es

Versión producida por el autor de la **información suplementaria** del artículo

publicado en:

This is the **electronic supporting information** (ESI) author version of a paper

published in:

ACS Nano 12.10 (2018): 10171-10177

DOI: https://doi.org/10.1021/acsnano.8b05056

Copyright: © 2018 American Chemical Society

One-Pot Preparation of Mechanically Robust, Transparent, Highly Conductive and Memristive Metal-Organic Ultrathin Film

Miriam Moreno-Moreno, Javier Troyano, Pablo Ares, Oscar Castillo, Christian A. Nijhuis, Li Yuan, Pilar Amo Ochoa, Salomé Delgado, Julio Gómez-Herrero, Félix Zamora and Cristina Gómez-Navarro

SUPPORTING INFORMATION

SI1. X-ray structure of $[Cu_2I_2(TAA)]_n$

X-ray diffraction data collections and structure determinations. They were done on a Bruker Kappa Apex II diffractometer using graphite-monochromated Mo-Kα radiation (λ = 0.71073 Å). The cell parameters were determined and refined by a least-squares fit of all reflections. A semi-empirical absorption correction (SADABS) was applied for all cases. All the structures were solved by direct methods using the SIR92 program and refined by full-matrix least-squares on F^2 including all reflections (SHELXL97). All calculations were performed using the WINGX crystallographic software package.[1] To solve the crystal structure of this compound it was necessary to introduce a great disorder on the position and occupation of the copper(I) metal centres and the thioacetamide ligand. The latter was refined imposing geometrical restraints on the planarity and C-C and C-N distances. The hydrogen atoms of these highly disordered thioacetamide ligands were not located. The iodide anions are the only atoms that remain non-disordered in the crystal structure. All the attempts to be able to reproduce the experimental data using lower symmetry space groups did not remove the presence of this disorder. All non-hydrogen atoms except those belonging to the thioacetamide ligand were refined anisotropically. Relevant data acquisition and refinement parameters are gathered in Table S1. CCDC 1568566-1568568 contain the supplementary crystallographic data for this paper.

These crystallographic features imply that the disorder cannot be explained as a mixture of two ordered models. In this compound, due to the great extent of the disorder, the amount of possible ordered models contributing to the mixture is huge and it has become impossible to provide a detail on all these ordered models. However, we provide some insight into three of these possible ordered models in which we can observe how the crystal structure is always build up by means of tetrahedral copper(I) metal centres. In all cases, the copper-iodide and copper-sulphur distances lay within their usual values.
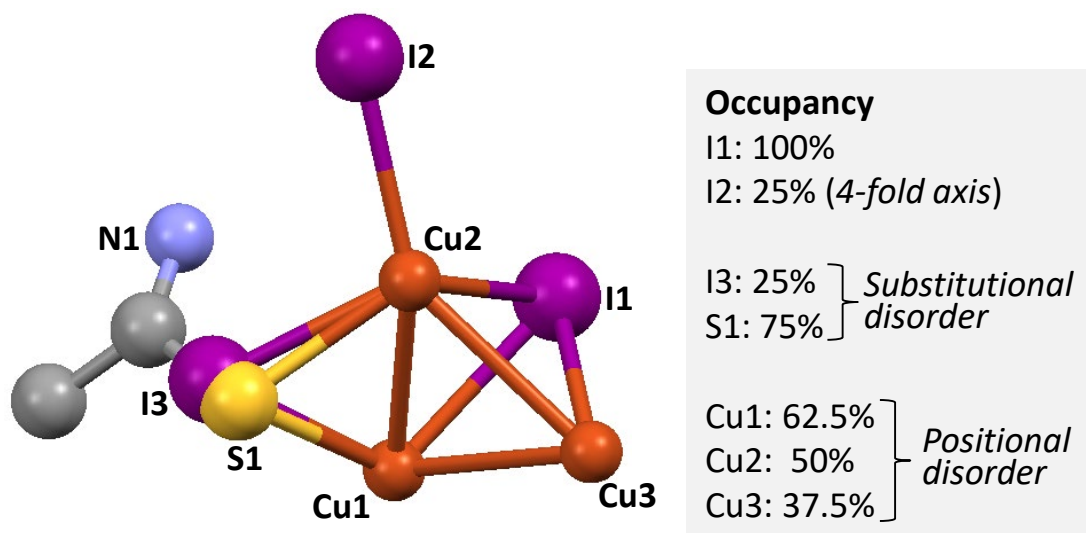

Occupancy
I1: 100%
I2: 25% (*4-fold axis*)

I3: 25% ⎤ *Substitutional*
S1: 75% ⎦ *disorder*

Cu1: 62.5% ⎤
Cu2: 50% ⎬ *Positional*
Cu3: 37.5% ⎦ *disorder*

Figure S1. View of the asymmetric unit of $[Cu_2I_2(TAA)]_n$ compound showing the occupation factors.
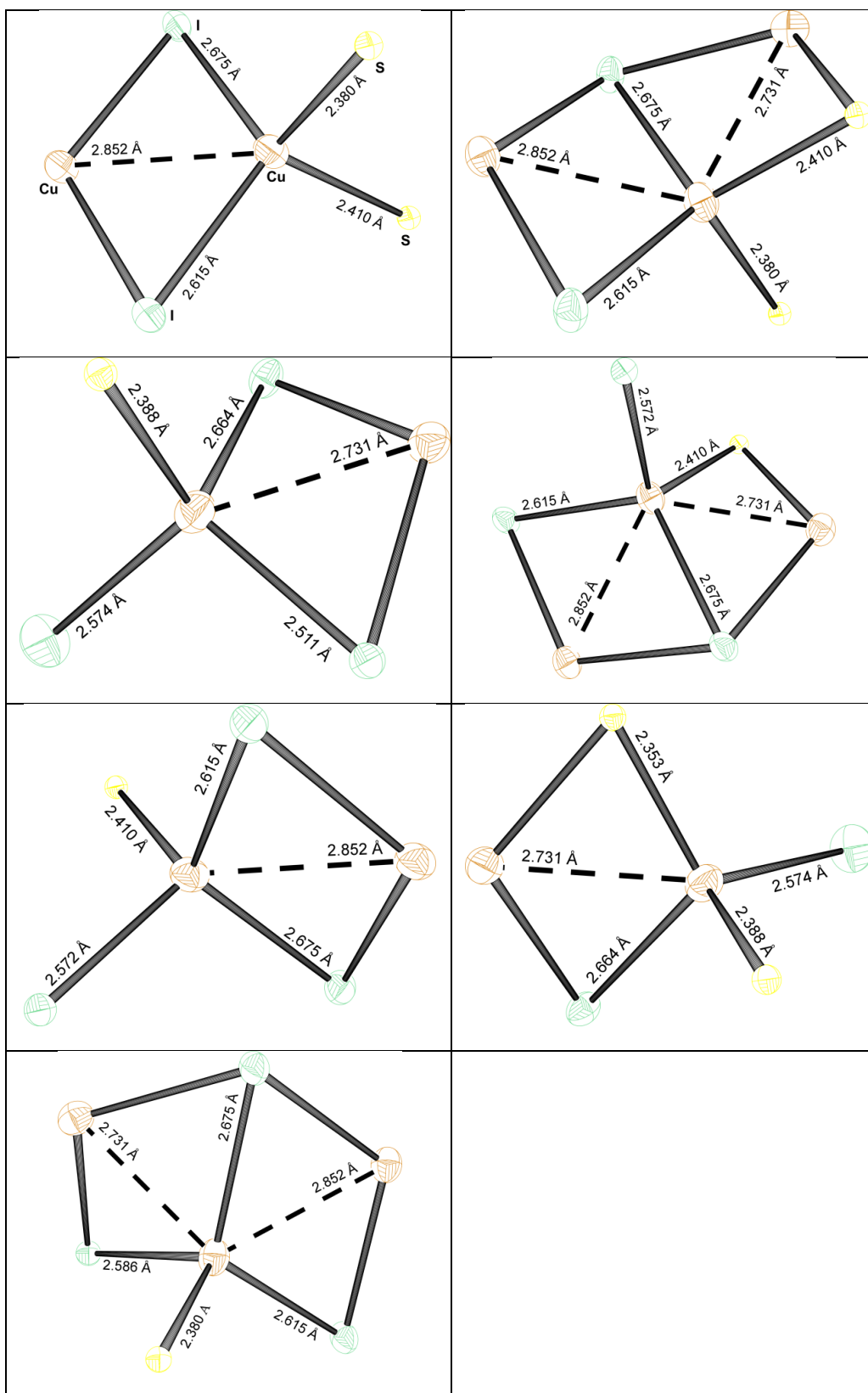
A MODEL

There are seven non-equivalent metal centres, all of them involve a tetrahedral coordination environment (with donor sets ranging from I_4, I_3S to I_2S_2). It must be emphasized also that for clarity purposes the non-sulphur atoms of the thioacetamide ligand have been omitted.
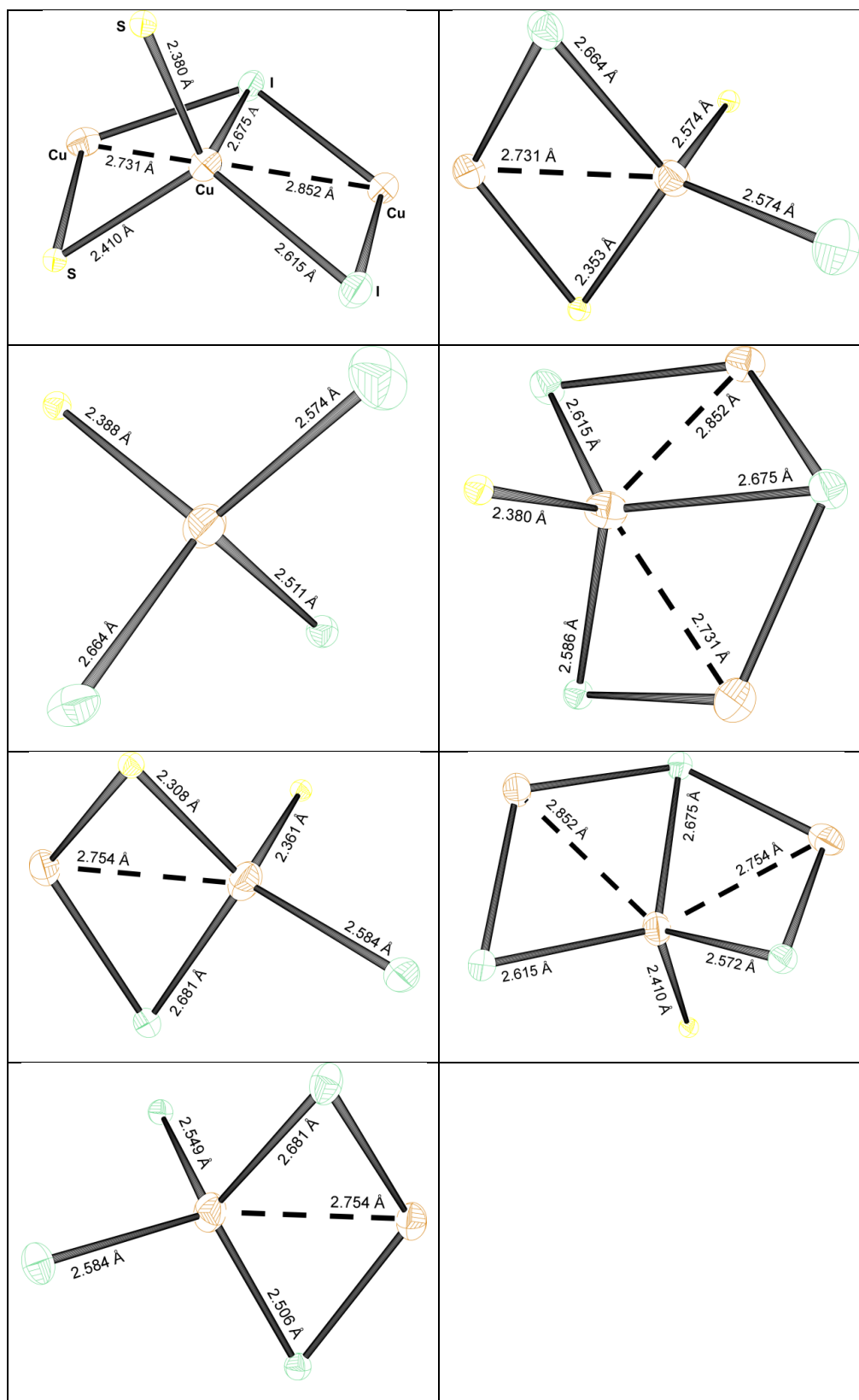
B MODEL

There are seven non-equivalent metal centres, all of them involve a tetrahedral coordination environment (with donor sets ranging from I_3S to I_2S_2). It must be emphasized also that for clarity purposes the non-sulphur atoms of the thioacetamide ligand have been omitted.

C MODEL

There are nine non-equivalent metal centres, all of them involve a tetrahedral coordination environment (with donor sets ranging from I_3S to I_2S_2). It must be emphasized also that for clarity purposes the non-sulphur atoms of the thioacetamide ligand have been omitted.
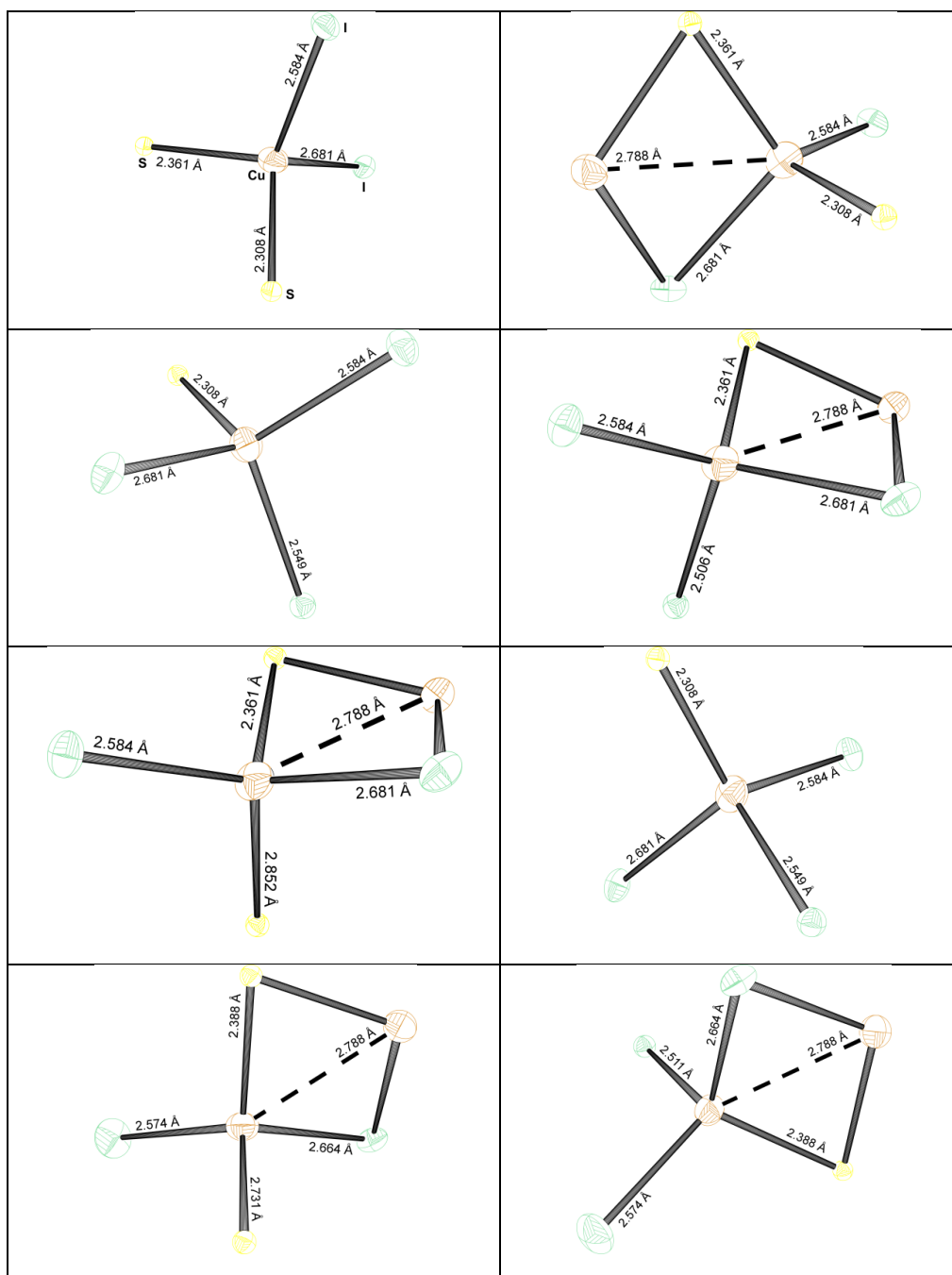
Table S1. Crystallographic data for $[Cu_2I_2(TAA)]_n$ compound at different temperatures.

	$[Cu_2I_2(TAA)]_{n100K}$	$[Cu_2I_2(TAA)]_{n200K}$	$[Cu_2I_2(TAA)]_{n296K}$
Empirical formula	$C_2H_5Cu_2I_2NS$	$C_2H_5Cu_2I_2NS$	$C_2H_5Cu_2I_2NS$
Formula weight	456.01	456.01	456.01
T (K)	100(2)	200(2)	296(2)
Crystal system	Tetragonal	Tetragonal	Tetragonal
Space group	$I\,4_1/a$	$I\,4_1/a$	$I\,4_1/a$
a (Å)	15.5848(7)	15.6261(18)	15.6634(3)
c (Å)	9.8950(5)	9.9155(13)	9.9466(2)
V (Å^3)	2403.4(2)	2421.1(6)	2440.32(11)
Z	12	12	12
R_{int}	0.1278	0.1241	0.1233
Reflections collected	10746	18868	19065
Independent reflections	1107	1245	1251
Reflections [I>2σ(I)]	976	1047	1014
Parameters	72	72	72
Restraints	9	9	9
Goodness of fit (S)[a]	1.077	1.076	1.065
R1[b] [I>2σ(I)]	0.0389	0.0488	0.0530
wR2[c] [I>2σ(I)]	0.1065	0.1293	0.1427
R1[b] [all data]	0.0438	0.0550	0.0609
wR2[c] [all data]	0.1091	0.1341	0.1484
Largest peak/hole (e$^-$ Å^3)	1.007/-1.780	2.337/-2.211	2.262/-2.001

[a] $S = [\sum w(F_0^2 - F_c^2)^2 / (N_{obs} - N_{param})]^{1/2}$ [b] $R1 = \sum ||F_0| - |F_c|| / \sum |F_0|$; [c] $wR2 = [\sum w(F_0^2 - F_c^2)^2 / \sum wF_0^2]^{1/2}$; $w = 1/[\sigma^2(F_0^2) + (aP)^2 + b]$ where $P = (max(F_0^2,0) + 2\,F_c^2)/3$ with a = 0.0554 ($[Cu_2I_2(TAA)]_n$ 100K), 0.0903 ($[Cu_2I_2(TAA)]_n$ 200K), 0.1015 ($[Cu_2I_2(TAA)]_n$ 296K) and b = 24.6784 ($[Cu_2I_2(TAA)]_n$ 100K), 2.2898 ($[Cu_2I_2(TAA)]_n$ 200K).

SI2. Electrical conductivity of bulk crystals

The electrical conductivity of crystals was measured by contacting them with graphite paint. Electrical characterization of obtained crystals showed that good quality crystals (selected by optical inspection of their morphology) presented conductivity values of 10^{-5} - 10^{-3} S/cm, but crystals with irregular morphology presented values up to 10 S/cm. To corroborate this suggested relation between crystallinity and electrical conductivity we tested good quality crystals (as indicated by X ray diffraction) and annealed them with the aim of amorphizating the structure, measuring electrical conductivity on the same crystal before and after annealing.
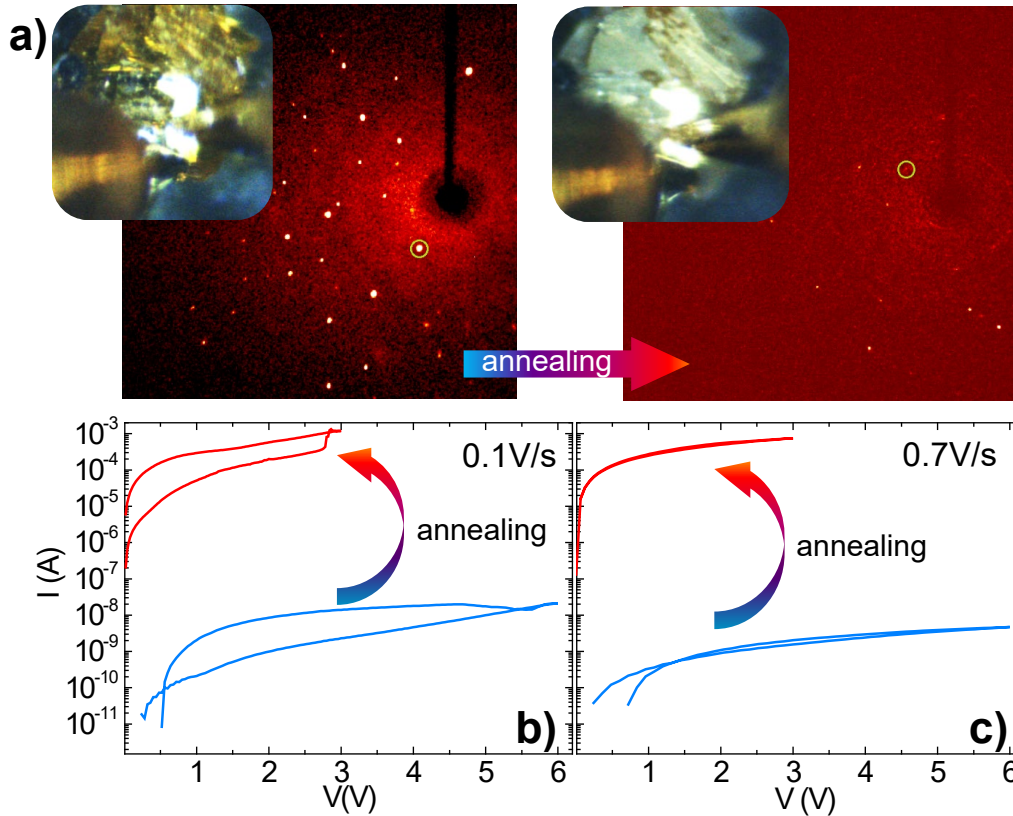

Figure S2. a) Intense and well defined diffraction spots are observed for a single crystal that has been kept under room conditions (left), but significantly less intense diffraction spots are found in the same crystal upon heating up to 70 °C (right), indicative of a loss of crystallinity. The (420) diffraction peak, in the centered tetragonal system I, has been encircled in both images for comparative purposes. In both cases the same exposure time was employed. The insets show optical images of the $[Cu_2I_2(TAA)]_n$ crystal before and after annealing from RT to 70 °C. The amorphization can be already appreciated in the brightness of the crystals. Panels b) and c) show IV curves on the crystal in a semi-log plot before (blue) and after (red) annealing for two sweep rates. The crystals showed an increase in conductivity of 5 orders of magnitude upon annealing and showed similar memristive character as the films.

SI3. XPS, IR spectra and thermal stability

Table S2. Binding energy values for different $[Cu_2I_2(TAA)]_n$ samples determined from XPS measurements.

Sample	Binding energy (eV)				
	$Cu2p_{3/2}$	$I3d_{5/2}$	S2p	N1s	C1s
$[Cu_2I_2(TAA)]_n$ powder	932.5	619.4	162.8	399.9	284.8 (65) 286.2 (35)
$[Cu_2I_2(TAA)]_n$ crystal	932.6	619.3	162.9	399.9	284.8 (67) 286.3 (33)
$[Cu_2I_2(TAA)]_n$ film	932.5	619.4	162.9	399.3	284.8 (65) 286.3 (35)
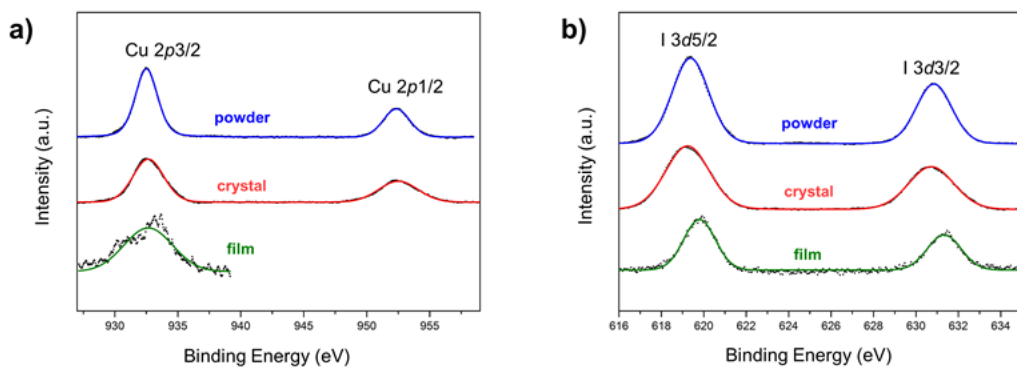
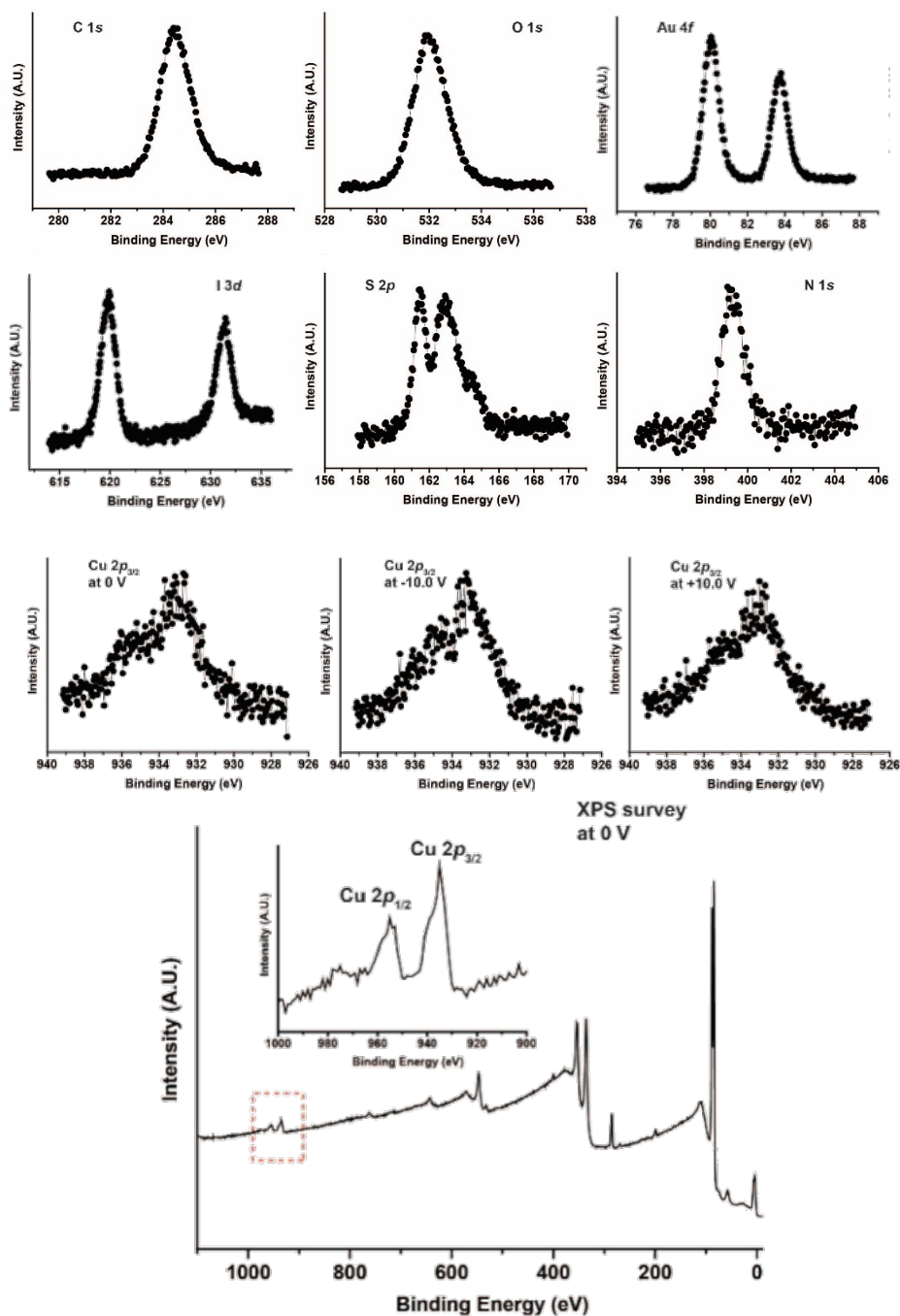**Figure S3.** XPS copper (a) and iodine (b) spectra of $[Cu_2I_2(TAA)]_n$ powder, crystal and film.

Figure S4. High resolution XPS spectra of $[Cu_2I_2(TAA)]_n$ films after applying 10 V characterized by synchrotron XPS. XPS of copper was registered at 0 and ±10 V.

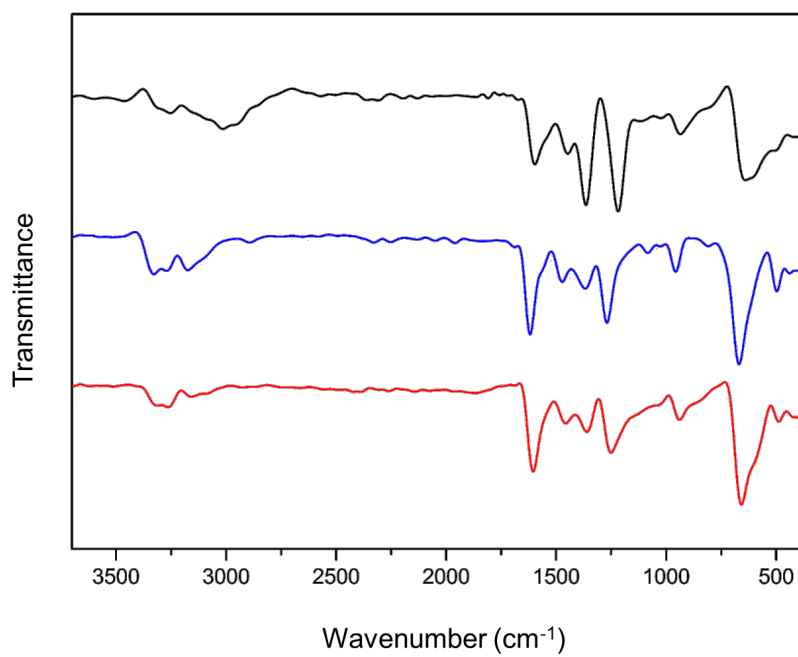**Figure S5.** FTIR spectra of $[Cu_2I_2(TAA)]_n$ crystals (black), powder (blue) and film (red). The spectra agree with an analogous structure for the $[Cu_2I_2(TAA)]_n$ crystals, powder and film.

For the thermal analysis of $[Cu_2I_2(TAA)]_n$ powder we first obtained the TGA curve and its first derivative. A weight loss of ~15 % was observed from 150 to 350 °C, reaching a plateau for higher temperatures (Figure S6a). The mass loss determined by TGA correlates with the loss of TAA molecules giving rise to a CuI residue (theoretical mass loss = 16 %). This transformation was confirmed by XRPD analysis of the product after heating $[Cu_2I_2(TAA)]_n$ powder at 200 °C for 1 h under inert atmosphere as shown in Figure S6b. Accordingly, we carried out a DSC experiment in this temperature range (from 25 °C to 350 °C) in order to determine the phase transition (T = 170 °C).
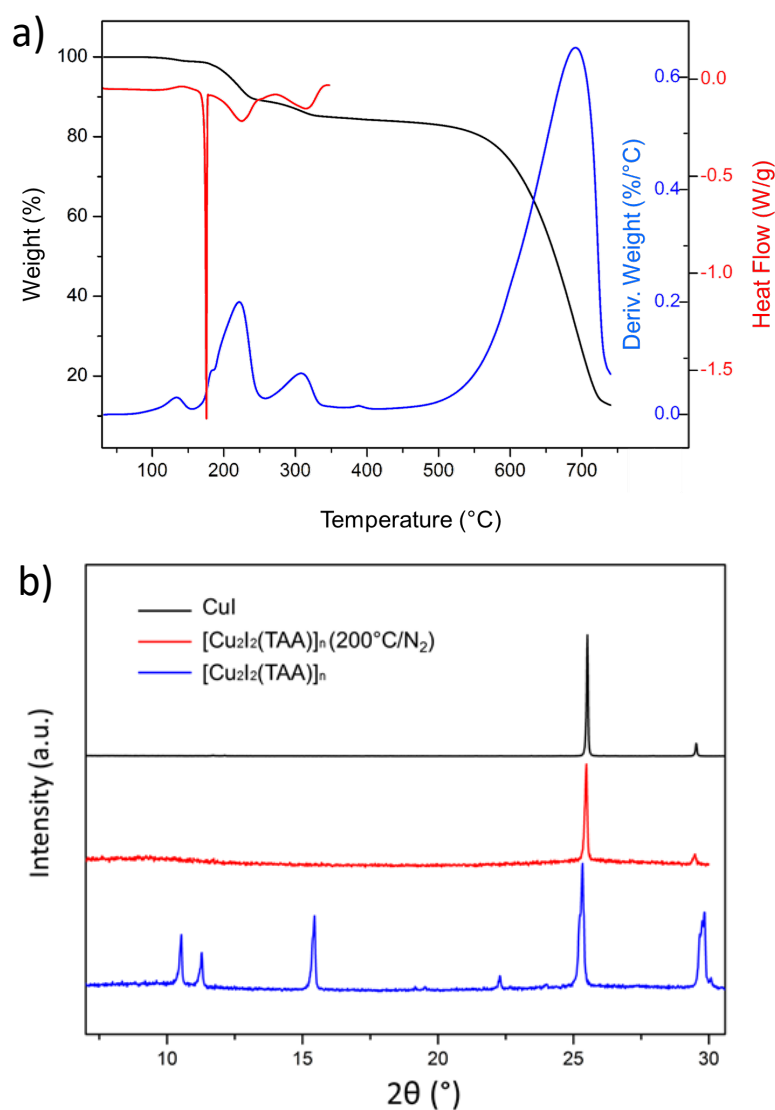

Figure S6. a) Thermal gravimetric analysis (TGA) (black), derivative TGA (blue) and differential scanning calorimetry (DSC) (red) of $[Cu_2I_2(TAA)]_n$ powder. b) X-ray powder diffraction of $[Cu_2I_2(TAA)]_n$ powder before (blue) and after (red) heating at 200 °C for 1 h under N_2 atmosphere compared to CuI (black).

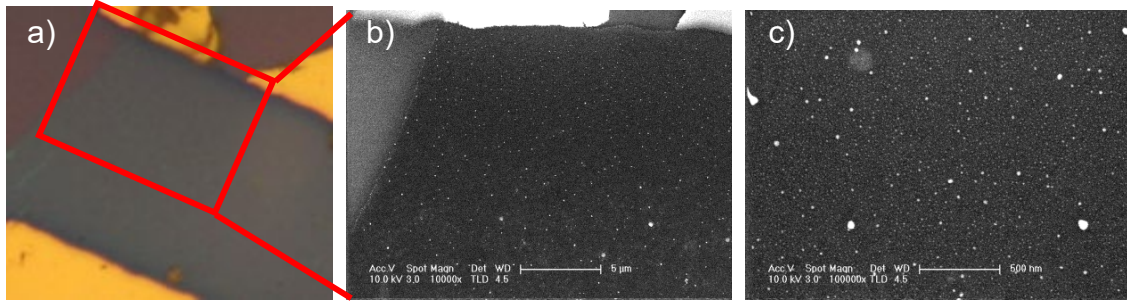## SI4. SEM images of films on substrates

Figure S7. a) 30×30 μm^2 optical image of an 8 nm thick film with gold electrodes on top. b) and c) SEM images with different magnifications of the film in panel a). While SEM images, as well as AFM, show some granular structure they allow discarding a nano-platelet structure as reported previously in similar metal-organic films.

SI5. Transversal electrical conductivity measurements

The bidimensional behaviour of our films in terms of electrical conductivity was confirmed by measuring transversal conductivity. Films collected on gold surfaces were contacted with Ga$_2$O$_3$/EGaIn[2] as top electrode (Figure S8a). The measured values of *ca*. 10^{-8} S/cm confirmed a tunnel conduction mechanism of the films in the out-of-plane direction (Figure S8b).
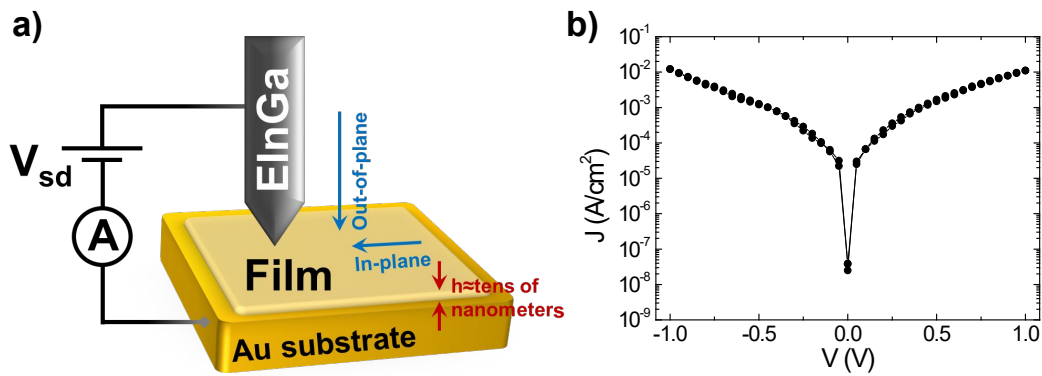

Figure S8. a) Experimental scheme used for the measurement of transversal (out-of-plane) conductivity. b) Current density *versus* bias voltage plot from which the transversal conductivity is obtained.
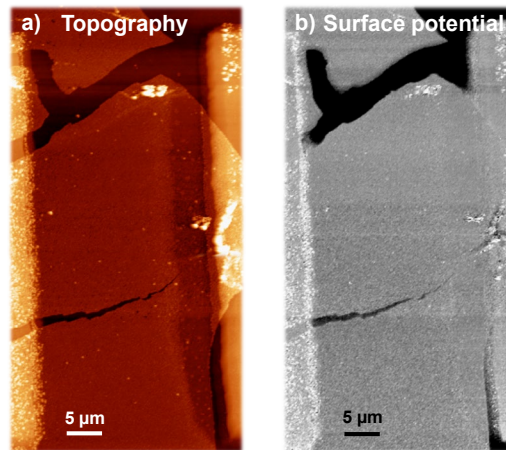
SI6. KPFM on low conductivity devices

Figure S9. Representative a) topography and b) surface potential map of a low conductivity device where the KPFM image appears featureless.
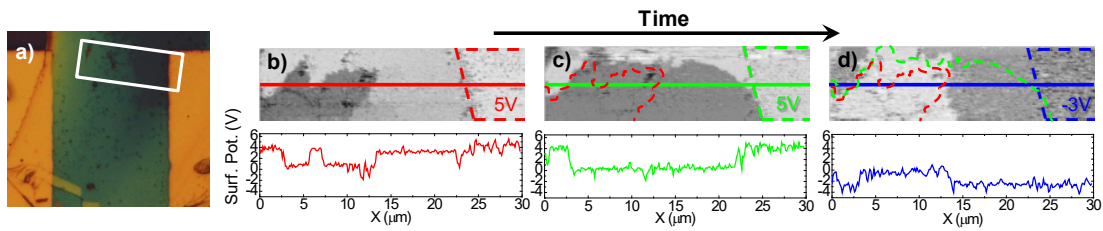
SI7. Grain boundary migration

Figure S10. a) Optical image of the device where subsequent images were acquired. Image size: $43 \times 38 \ \mu m^2$. b, c) Surface potential maps of the region of the device marked in panel a) while 5 V were applied to the right electrode (electrode is indicated by dotted lines). The left electrode is located several microns to the left of each image. It was not scanned in order to minimize the image acquisition time. The time lapse between panels b) and c) is 3 minutes. d) Surface potential map of the same region with -3 V applied to the right electrode. The time between panels c) and d) was 3 minutes. Lower panels are the corresponding profiles along the lines in each image. In c) and d) the borders of different surface potential regions of the previous images are marked with dashed coloured lines. The topography of the studied area remains the same during all the KPFM measurements.

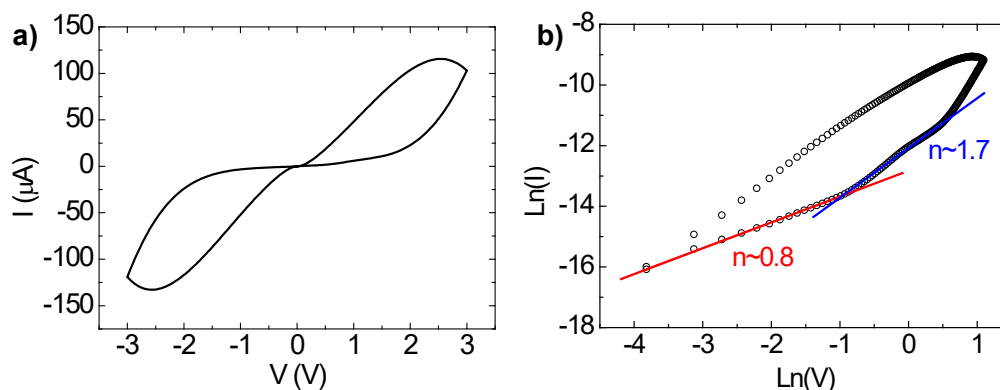## SI8. *IV* curve fitting to Space Charge Limited Current (SCLC) model

Figure S11. a) *IV* curve of a representative film acquired at 0.062 V/s. b) The Ln-Ln representation of the positive-bias loop of the *IV* curve plotted in a) together with linear fittings showing the slopes (exponent in I $\propto$ V^n) of two characteristic regions of typical SCLC:[3] an ohmic part at low voltages and a second region with I $\propto$ V^2 where the traps begin to be filled with the injected carriers. In the third region with $n >$ 2 all traps are filled up, so the subsequently injected carriers can move in the dielectric film causing the subsequent current increasing.

References

1.   Farrugia, L. WinGX Suite for Small-Molecule Single-Crystal Crystallography. *J. Appl. Crystallo.* **1999,** *32*, 837-838.

2.   Chiechi, R. C.; Weiss, E. A.; Dickey, M. D.; Whitesides, G. M. Eutectic Gallium-Indium (EGaIn): A Moldable Liquid Metal for Electrical Characterization of Self-Sssembled Monolayers. *Angew. Chem. Int. Ed.* **2008,** *47*, 142-144.

3.   Chiu, F. C. A Review on Conduction Mechanisms in Dielectric Films. *Adv. Mater. Sci. Engin.* **2014,** Art. Num. 578168.